Cavitation Bubble Collapse Near a Heated Wall and Its Effect on the Heat Transfer

Bin Liu
Institute of Engineering Thermophysics,
Chinese Academy of Sciences,
Beijing 100190, China;
University of Chinese Academy of Sciences,
Beijing 100080, China

Jun Cai[1]
e-mail: caijun@mail.etp.ac.cn

Xiulan Huai

Fengchao Li

Institute of Engineering Thermophysics,
Chinese Academy of Sciences,
Beijing 100190, China

In the present work, a numerical investigation on the mechanism of heat transfer enhancement by a cavitation bubble collapsing near a heated wall has been presented. The Navier–Stokes equations and volume of fluid (VOF) model are employed to predict the flow state and capture the liquid-gas interface. The model was validated by comparing with the experimental data. The results show that the microjet violently impinges on the heated wall after the bubble collapses completely. In the meantime, the thickness of the thermal boundary layer and the wall temperature decrease significantly within the active scope of the microjet. The fresh low-temperature liquid and the impingement brought by the microjet should be responsible for the heat transfer reinforcement between the heated wall and the liquid. In addition, it is found that the impingement width of the microjet on the heated wall always keeps 20% of the bubble diameter. And, the enhancement degree of heat transfer significantly depends on such factors as stand-off distance, saturated vapor pressure, and initial bubble radius. [DOI: 10.1115/1.4024071]

Keywords: cavitation, near-wall bubble collapse, heat transfer enhancement, microjet, VOF

1 Introduction

Cavitation phenomenon is the rapid formation and collapse of bubbles when the local static pressure in the liquid is lower than the saturated vapor pressure. The near wall bubble collapse will induce shock waves and the high speed microjet, which are thought to be the main factors causing serious structural damage in hydraulic devices. Also, some researchers proposed that this unique flow pattern can enhance heat transfer between the liquid and solid boundary [1].

Many theoretical and experimental investigations on the dynamic behaviors of cavitation bubbles have been conducted. Rayleigh [2] calculated the collapse of a spherical bubble in an infinite body, which is the first serious scientific study for the bubble dynamic problem. However, because his work was based on the assumptions of empty bubble and incompressible liquid, the obtained collapse pressure tends to be infinite as the bubble collapses completely. In view of this point, Plesset [3] further considered some actual situations such as the effects of liquid viscosity and surface tension. Calculation results obtained by this improved model were quite close to the data from experiments. Subsequently, Gilmore [4] took into account the influence of liquid compressibility on cavitation bubble dynamics and obtained more realistic results, but the error was very large under a high Mach number. Afterward, the finite difference scheme based on the cylindrical coordinates was introduced to simulate the collapse of an initially spherical vapor bubble in the neighborhood of a solid boundary, and the changes of the gas-liquid interface were clearly visualized [5]. By showing the bubble paths during the growth and subsequent collapse, Blake and Gibson [6] found that the re-entrant jet was a possible hydrodynamic cause for cavitation erosion. Recently, Samiei et al. [7] studied the collapse of a bubble near a rigid boundary by using the VOF method to track the interface. By analyzing the effects of such factors as surface tension, initial bubble radius, and ambient pressure, they revealed that surface tension was a more significant factor responsible for the collapse shape and jet pattern of the smaller bubble under a low pressure. Johnsen and Colonius [8] used the WENO scheme to simulate the collapse of a gas bubble in water and capture the interface, and the shock propagation in the collapse was obtained. In addition, they proposed that the surface tension and viscous effect may be important for small bubbles.

Naude and Ellis [9] experimentally studied bubble dynamics with high speed photography, and the microjet in collapse was observed. Benjamin and Ellis [10] further conducted a few experiments to observe features of the unsymmetrical collapse of vapor bubbles and found that the bubble generated in the free fall box was a means for creating gravity-free conditions. Later, Tomita and Shima [11] carried out a more detailed experiment to study the formation of the impulsive pressure and its general features during the bubble collapse, and they thought that the impulsive pressure was closely relative to the plastic deformation of the material. Based on these previous works, the formation of a high-speed liquid jet and the emission of shock waves at the moment of collapse were experimentally investigated [12,13], and the cavitation damage on the material surface was observed when the bubble was generated at a distance away from the solid boundary that is less than twice its maximum radius. By experimentally investigating the collapse of a single bubble at different stand-off distances away from the solid boundary, Yang et al. [14] found that the Kelvin–Helmholtz vortices would be formed when the liquid jet was induced by the pressure wave.

Previous studies mainly focus on the bubble behavior dynamics, and there are few investigations on the cavitation enhanced heat transfer and its mechanism until now. Schneider et al. [15] experimentally investigated the force convection heat transfer with hydrodynamic cavitation in microchannels. They found that the cavitating flow has a significant higher heat transfer coefficient than the noncavitating flow. Nevertheless, they did not give the microscopic mechanism of cavitation enhanced heat transfer. Natural convection heat transfer of liquid in a square enclosure with and without acoustic cavitation has been numerically and experimentally studied [16,17]. The heat transfer enhancement was realized by means of acoustic cavitation and had the best effect when the head of the ultrasonic transducer was over the midpoint of the heating circular tube. Glancing at the existing research profile, many investigations have been conducted from a macro perspective view, which still fails to reveal the microscopic

[1]Corresponding author.

Contributed by the Heat Transfer Division of ASME for publication in the JOURNAL OF HEAT TRANSFER. Manuscript received October 7, 2012; final manuscript received March 14, 2013; published online November 5, 2013. Assoc. Editor: W. Q. Tao.

mechanism of cavitation enhanced heat transfer. The lack of the understanding for the mechanism seriously hinders the practical applications of hydrodynamic cavitation as a cooling technique. In order to better understand the determined factors influencing heat transfer efficiency under the cavitation, the collapse behavior of a single bubble near a heated solid wall and its effect on the heat transfer are analyzed. In the present work, the VOF method is used to capture the interface between phases. Changes of liquid-gas interface, microjet flow pattern, and temperature distribution of the wall are exhibited to reveal the basic principle of cavitation enhanced heat transfer. In addition, the effects of such factors as the nondimensional stand-off distance, saturated vapor pressure, and bubble initial radius are discussed in details.

2 Theoretical Model

In this study, it is assumed that the flow field contains two immiscible phases without mass transfer, and the flow pattern is laminar. The cavitation bubble is considered to be filled with compressible air and surrounded by incompressible water. The collapse of a bubble in stationary water is thought to be axially symmetrical; thus, the corresponding governing equations for both phases in an axisymmetric coordinate are solved. The mass conservation equation for the mixture is given by

$$\frac{\partial \rho}{\partial t} + \nabla \cdot (\rho \vec{v}) = 0 \tag{1}$$

where ρ is the density of the mixture, $\vec{v}$ is the velocity, and t is the time. For the axisymmetric flow, Eq. (1) is described by

$$\frac{\partial \rho}{\partial t} + \frac{\partial}{\partial x}(\rho v_x) + \frac{\partial}{\partial r}(\rho v_r) + \frac{\rho v_r}{r} = 0 \tag{2}$$

where x is the axial coordinate, r is the radial coordinate, v_x is the axial velocity, and v_r is the radial velocity.

A single set of momentum equations, which is solved throughout the domain and shared by the two phases, can be expressed as

$$\frac{\partial}{\partial t}(\rho \vec{v}) + \nabla \cdot (\rho \vec{v}\vec{v}) = -\nabla p + \nabla \cdot \left(\vec{\tau}\right) + \vec{F} \tag{3}$$

where p is the total pressure, $\vec{F}$ is a surface tension contribution term, and $\vec{\tau}$ is the stress tensor given by

$$\vec{\tau} = \mu \left[(\nabla \vec{v} + \nabla \vec{v}^T) - \frac{2}{3} \nabla \cdot \vec{v} I \right] \tag{4}$$

where μ is the dynamic viscosity, and I is the unit tensor. As a source term in the momentum equation, $\vec{F}$ can be calculated by the continuum surface force (CSF) model proposed by Brackbill et al. [18]. According to the divergence theorem, $\vec{F}$ can be reformulated into an equivalent volume force as follows:

$$\vec{F} = \sigma \frac{\rho \kappa \nabla \alpha_g}{0.5(\rho_g + \rho_l)} \tag{5}$$

where σ is the surface tension coefficient and takes 0.072 N/m in this work, and $\kappa = \nabla \cdot (\vec{n}/|\vec{n}|)$ is the curvature of the phases interface. The conservation forms of the axial and radial momentum equations in an axisymmetric coordinate are given by

$$\begin{aligned} &\frac{\partial}{\partial t}(\rho v_x) + \frac{1}{r}\frac{\partial}{\partial x}(r\rho v_x v_x) + \frac{1}{r}\frac{\partial}{\partial r}(r\rho v_r v_x) \\ &\quad = -\frac{\partial p}{\partial x} + \frac{1}{r}\frac{\partial}{\partial x}\left[r\mu \left(2\frac{\partial v_x}{\partial x} - \frac{2}{3}(\nabla \cdot \vec{v}) \right) \right] \\ &\qquad + \frac{1}{r}\frac{\partial}{\partial r}\left[r\mu \left(\frac{\partial v_r}{\partial x} + \frac{\partial v_x}{\partial r} \right) \right] + F_x \end{aligned} \tag{6}$$

$$\begin{aligned} &\frac{\partial}{\partial t}(\rho v_r) + \frac{1}{r}\frac{\partial}{\partial x}(r\rho v_x v_r) + \frac{1}{r}\frac{\partial}{\partial r}(r\rho v_r v_r) \\ &\quad = -\frac{\partial p}{\partial r} + \frac{1}{r}\frac{\partial}{\partial r}\left[r\mu \left(2\frac{\partial v_r}{\partial r} - \frac{2}{3}(\nabla \cdot \vec{v}) \right) \right] \\ &\qquad + \frac{1}{r}\frac{\partial}{\partial x}\left[r\mu \left(\frac{\partial v_r}{\partial x} + \frac{\partial v_x}{\partial r} \right) \right] - 2\mu \frac{v_r}{r^2} + \frac{2}{3}\frac{\mu}{r}(\nabla \cdot \vec{v}) + F_r \end{aligned} \tag{7}$$

where $\nabla \cdot \vec{v} = (\partial v_x/\partial x) + (\partial v_r/\partial r) + (v_r/r)$.

The energy equation is

$$\frac{\partial}{\partial t}(\rho E) + \nabla \cdot (\vec{v}(\rho E + p)) = \nabla \cdot \left(k \nabla T_f\right) \tag{8}$$

where k is the effective conductivity, T_f is the fluid temperature, and E is the total energy in the fluid element and can be expressed as

$$E = \frac{\alpha_g \rho_g E_g + \alpha_l \rho_l E_l}{\alpha_g \rho_g + \alpha_l \rho_l} \tag{9}$$

where α is the volume fraction. The subscripts "l" and "g" represent the liquid phase and gas phase, respectively.

For a 2D axisymmetric geometry, the energy equation has the following form:

$$\begin{aligned} &\frac{\partial(\rho E)}{\partial t} + \frac{\partial}{r\partial r}(r v_r(\rho E + p)) + \frac{\partial}{\partial x}(v_x(\rho E + p)) \\ &\quad = \frac{\partial}{\partial x}\left(k\frac{\partial}{\partial x} T_f \right) + \frac{1}{r}\frac{\partial}{\partial r}\left(rk\frac{\partial T_f}{\partial r} \right) \end{aligned} \tag{10}$$

The VOF model is designed for two or more immiscible fluids based on the Eulerian mesh, where the position of the interface between two fluids is of interest [19]. In the present work, the motion of liquid-gas interface between two fluids is tracked throughout the domain by solving a continuity equation for the volume fraction of the second phase, which is considered to be water in this work. The volume fraction equation has the following form:

$$\frac{\partial \alpha_l}{\partial t} + \vec{v} \cdot \nabla \alpha_l = 0 \tag{11}$$

The volume fraction of air is computed based on the following constraint

$$\alpha_l + \alpha_g = 1 \tag{12}$$

The average density and absolute viscosity in each control volume are calculated according to the volume fraction values of air and water, which are expressed as

$$\rho = \rho_l \alpha_l + \rho_g \alpha_g \tag{13}$$

$$\mu = \mu_l \alpha_l + \mu_g \alpha_g \tag{14}$$

Air (primary phase) inside the bubble is considered to be compressible; thus, the variation of its density accords with the ideal gas law

$$\rho_g = \frac{p M_w}{R T_f} \tag{15}$$

where R is the gas constant, and M_w is the molecular weight of the gas.

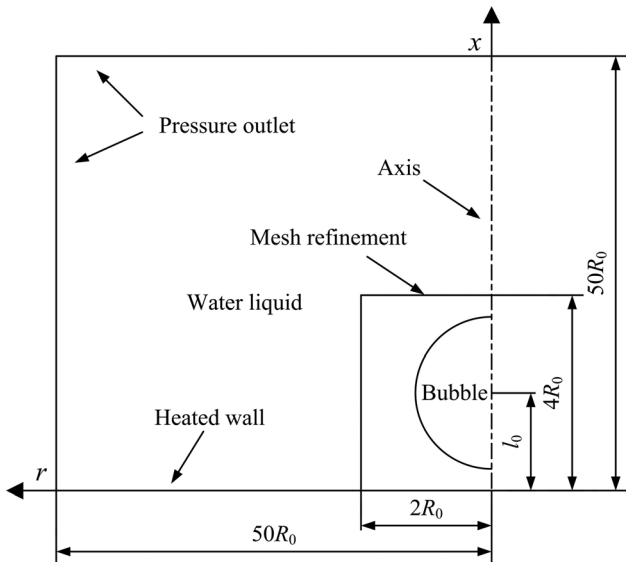

Fig. 1 Calculation domain

3 Physical Model and Numerical Method

A structured 2D axisymmetric grid is adopted to simulate the bubble collapse near a heated solid wall, as shown in Fig. 1. The bottom of the calculation domain is a stationary solid wall, on which a constant heat flux with $q = 3.5 \times 10^6\,\mathrm{W/m^2}$ is imposed. For the left and top far-field boundaries, the pressure outlet boundary conditions are adopted and set as 100 kPa. The axial boundary condition is employed for the centerline. The whole domain is divided into two parts, general calculation area and mesh refinement area. The width of the calculation domain is set as $50R_0 \times 50R_0$ (R_0 is the initial bubble radius). The meshes are refined in the area of $2R_0$ (r direction) $\times 4R_0$ (x direction) so as to capture the change of the liquid-gas interface. For the convenience of the analysis, the nondimensional stand-off distance (γ) is introduced and defined as l_0/R_0, where l_0 is the initial distance from the bubble center to the wall.

In the calculation, air inside the bubble is chosen as the primary phase and conforms to the ideal gas law. The initial gas pressure inside the bubble is set as the saturated vapor pressure of water corresponding to the operating temperature. The operating pressure is set to zero, and the location of reference pressure is located at the point where two pressure outlet boundaries intersect. In the present work, the gravity is not considered. Other parameters are the default values of physical properties. The PISO algorithm is used for the pressure-velocity coupling. The pressure is discretized with the PRESTO scheme. The VOF equation is explicitly solved with the geometric reconstruction scheme. The second order upwind scheme is used to discretize the momentum and energy conservation equations. An adaptive time step has been implemented to improve the computational efficiency. Based on the maximum Courant number near the VOF interface, the variable time step is in the range of $5 \times 10^{-10} \sim 1 \times 10^{-9}$ s. The convergence criterion is 10^{-6} for the continuity and momentum equations and 10^{-9} for the energy equation.

4 Solution Verification

4.1 Grid Independence. During the collapse of the cavitation bubble, the interface of the bubble shows a significant change in an incredibly short period of time, and the resultant high speed jet pattern is very complex. Therefore, it is necessary to select an appropriate element size for grids. In order to capture the change of the interface and ensure the grid independence at the same time, three kinds of grid number, i.e., 8×10^4, 3.2×10^5, and 1.28×10^6 in the mesh refinement area are used. In the calculation, the initial bubble radius R_0 is 1.45 mm, and the saturated vapor pressure is set as 3 kPa. Both initial liquid temperature and air temperature are 298 K, and $\gamma = 1.6$ is adopted. In the model verification section, the heat flux is not imposed on the wall boundary. Figure 2 shows the distribution of the local jet velocity on the axis when the jet pierces the bubble. The results under 3.2×10^5 and 1.28×10^6 cells are very close, and the maximum deviation is less than 2%, so the grid number of 3.2×10^5 in the refinement area can meet the accuracy requirement and is adopted in the subsequent computations.

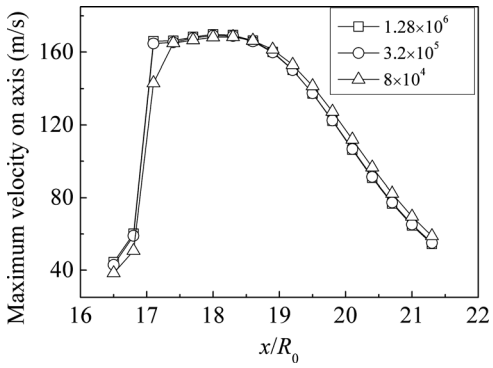

Fig. 2 Grid independency test

4.2 Comparison With Experimental Results. Figure 3 indicates the comparison of the present bubble profiles with the experimental results in the literature [12]. The bubble profiles obtained by the present theoretical model are very similar to the photographs taken in the experiment, which demonstrates the correctness and reliability of the present model. Therefore, the present model can be used to predict and analyze the collapse and rebound of the cavitation bubble near a heated wall and the resultant effect on the heat transfer between the liquid and solid wall.

5 Results and Discussion

The collapse behaviors of the bubble are influenced by the nondimensional stand-off distance, saturated vapor pressure, and

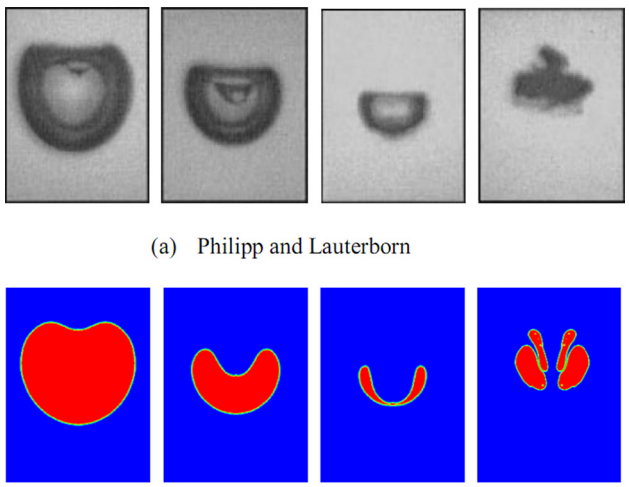

Fig. 3 The comparison of bubble profiles with the experimental results. (*a*) Philipp and Lauterborn [12], and (*b*) present results.

Table 1 Calculation cases

Cases	P_v (kPa)	γ	R_0 (mm)	T_f (K)
1	3	1.1	0.1	298
2	3	1.4	0.1	298
3	3	1.7	0.1	298
4	3	1.1	0.15	298
5	3	1.1	0.2	298
6	4	1.1	0.1	303
7	5	1.1	0.1	315

initial bubble radius. In the present work, seven different cases are employed to analyze the effects of these factors, as shown in Table 1.

5.1 Bubble Collapse Behaviors Near the Heated Wall. In this section, those parameters shown in case 1 are selected to simulate the collapse behaviors of the bubble near a heated wall. In order to facilitate the comparison for the calculation results under different conditions, a nondimensional time t^* is introduced and expressed as

$$t^* = t/t_c \tag{16}$$

where t_c is the collapse time, which is the moment that the bubble is just penetrated by the jet and equals 1.09462 μs for case 1. Figure 4 shows the bubble profiles at different t^*. At the beginning, a spherical bubble is patched in stationary water. Surrounded by high pressure water, the bubble is squeezed from the left and right sides to the middle, and forms the "egg" shape. Subsequently, the gas-liquid interface on the top side of the bubble shrinks more rapidly than that on the bottom side. Therefore, a hollow is formed on the upper interface of the bubble. At $t^* = 1$, the bubble is just penetrated by the liquid jet and turns into a ring cavity, and the microjet velocity on the axis reaches the maximum at this moment. After that, the bubble continues to shrink and begins to rebound when getting the minimum size. Figure 5 shows the temperature distributions on the heating surface at different t^*. For $t^* \leq 1$, the wall temperature is nearly the same along the radial direction (r direction) and gradually rises due to the heating effect as time goes by. After the bubble is penetrated by the jet, the wall temperature begins to gradually decrease, especially in the range of $-0.02\,\text{mm} < r < 0.02\,\text{mm}$. The solid surface facing the jet flow is known as the stagnation region. It can be seen at $t^* = 1.0286$ that the temperature values in the stagnation region are far lower than those in the other wall regions. The distribution of the near-wall flow field at $t^* = 1.0286$ is shown in Fig. 6. The microjet moves towards the wall and spreads around along the wall after reaching the solid boundary. At the same time, the rotating flow can be observed near the upper surface of the ring cavity, and the active scope of the microjet equals the range of heat transfer enhancement. Therefore, the heat transfer enhancement should be attributed to the impingement of the microjet.

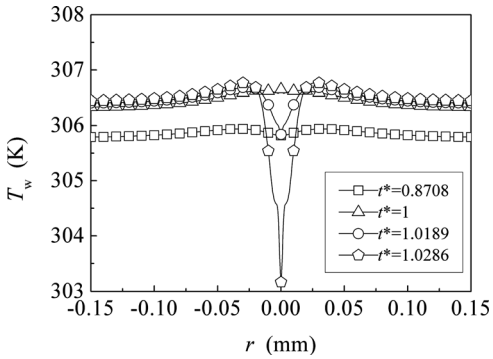

Fig. 5 Temperature distributions on the solid wall at different t^*

In Fig. 7, the near-wall temperature field at $t^* = 1.0286$ is depicted. It can be seen that the thickness of the thermal boundary layer in the stagnation region drops obviously compared with the neighborhood wall surface. The microjet excludes the high-temperature liquid in the thermal boundary layer, and fresh low-temperature liquid enters into it at the same time. Therefore, heat transfer between solid wall and liquid is improved. In the present work, the collapse of a single bubble is studied, so the heat transfer enhancement region is limited in the active scope of the microjet. If multiple cavitation bubbles (bubble cluster) collapse simultaneously near the solid wall, the whole heating surface will be impinged by the microjet, which would bring a larger area for the heat transfer enhancement.

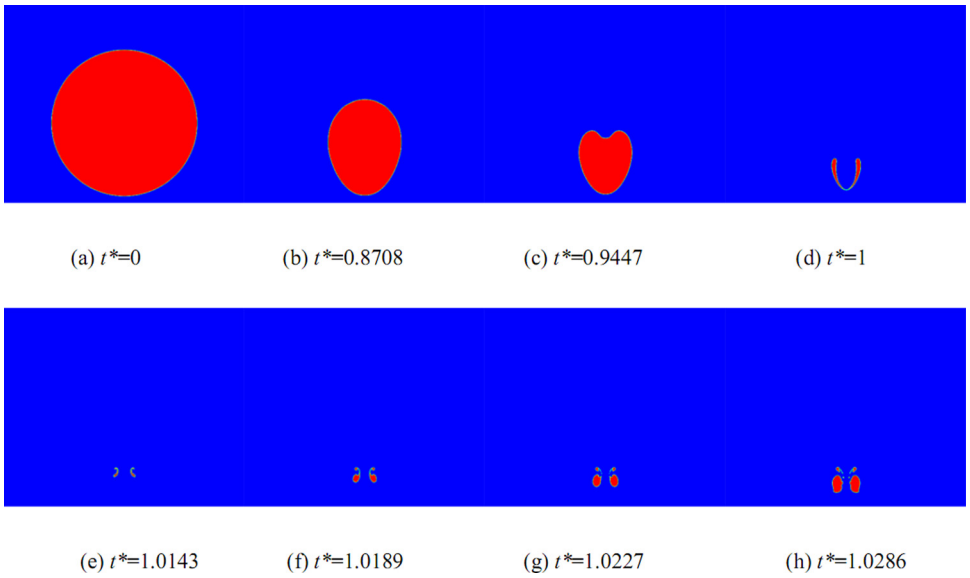

Fig. 4 Bubble profiles at different t^*. (*a*) $t^* = 0$, (*b*) $t^* = 0.8708$, (*c*) $t^* = 0.9447$, (*d*) $t^* = 1$, (*e*) $t^* = 1.0143$, (*f*) $t^* = 1.0189$, (*g*) $t^* = 1.0227$, and (*h*) $t^* = 1.0286$.

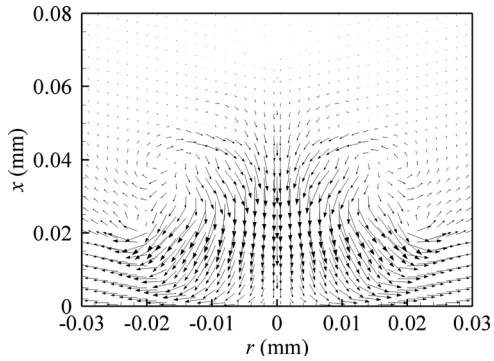

Fig. 6 The near-wall microjet vector fields at $t^* = 1.0286$

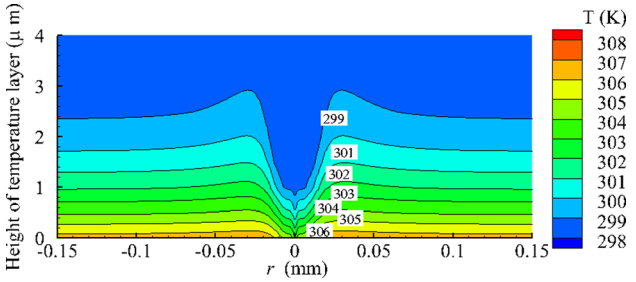

Fig. 7 The near-wall temperature field at $t^* = 1.0286$

Table 2 Maximum jet velocities on the axis and collapse time at different γ

γ	1.1	1.4	1.7
v_{max} (m/s)	128.021	150.549	188.419
t_c (μs)	1.09462	1.05191	1.02918

5.2 Influence of the Stand-Off Distance. The effect of the nondimensional stand-off distance (γ) on the bubble collapse is realized by changing the distance from the bubble center to the wall, and the other parameters remain the same as those in case 1. The maximum jet velocities on the axis and the collapse time at different stand-off distances are shown in Table 2. It can be seen that the maximum jet velocity on the axis rises obviously with the increase of γ, which means higher collapse strength. By contrast, the collapse time (t_c) is shortened from 1.09462 μs to 1.02918 μs. This indicates that the bubble shrinks more rapidly for a longer stand-off distance.

As mentioned above, the bubble collapse time varies with the different calculation conditions, which means that the solid wall will be subjected to the different heating time. In addition, the initial liquid temperature is differently set in order to evaluate the effect of the saturated vapor pressure. Therefore, the wall temperature is not the same under various situations. To easily analyze the effects of various factors under the same level and intuitively characterize the degree of the heat transfer enhancement, a dimensionless temperature is introduced

$$\eta = \frac{T_w}{T_{wr}} \tag{17}$$

Here, T_{wr} is the wall temperature at the reference point of $r = 0.5$ mm where heat transfer is free from the impingement of the microjet. A value of η less than 1.0 means that heat transfer is intensified, and the lower η is, the more obvious the heat transfer enhancement is. Figure 8 shows the time-dependent changes of

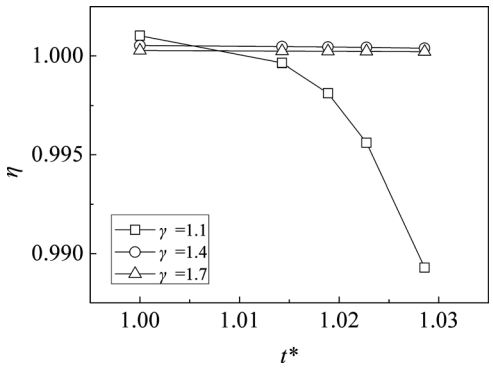

Fig. 8 Changes of the dimensionless temperature at the central point of the wall for different γ

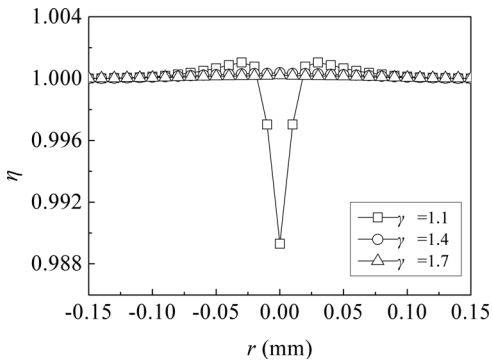

Fig. 9 Distributions of the dimensionless temperature on the solid wall under different γ at $t^* = 1.0286$

the dimensionless temperature at the central point of the solid wall ($r = 0$ mm) under the different γ. For all the stand-off distances, the heat transfer between solid wall and liquid has not been enhanced before the bubble collapses completely. After this, the situation continues at the stage of bubble rebound stage for $\gamma = 1.4$ and 1.7. On the contrary, the heat transfer is significantly enhanced during this period when $\gamma = 1.1$. This shows that a large stand-off distance for the cavitation bubble away from the heated wall would not bring the heat transfer enhancement. Although the higher collapse strength can be obtained for the longer stand-off distance, the microjet must go through a longer distance to reach the heated solid wall. The impact of the microjet on the solid wall would be considerably weaken and even disappear due to the cushioning effect of the liquid. Figure 9 shows the distributions of the dimensionless temperature on the heating surface for the different γ values at $t^* = 1.0286$. For $\gamma = 1.1$, the improvement of heat transfer can be observed around the central point of the solid wall. However, for $\gamma = 1.4$ and 1.7, the temperature on the whole solid wall is uniform, which indicates the heated wall is free from the impingement of the microjet. Although the velocity of the microjet increases with the increase of γ (see Table 2), it would attenuate rapidly after a long distance traveled in the liquid. From the theoretical point of view, there must be an optimal γ value for the heat transfer enhancement. In order to find the determined optimal value, it needs to be further investigated by means of experiment and theoretical analysis in future.

5.3 Influence of the Saturated Vapor Pressure. The calculations have been done with the saturated vapor pressure at 3 kPa, 4 kPa, and 5 kPa. The thermal physical parameters for two phases are determined according to the corresponding temperatures of 298 K, 303 K, and 315 K, respectively. The other parameters are the same as those in case 1. Table 3 shows the maximum jet

Table 3 Maximum jet velocities on the axis and collapse time for the different saturated vapor pressures

P_v (kPa)	3	4	5
v_{max} (m/s)	128.021	120.686	117.905
t_c (μs)	1.09462	1.10636	1.11433

Table 4 Maximum jet velocities on the axis and collapse time under the different bubble radii

R_0 (mm)	0.1	0.15	0.2
v_{max} (m/s)	128.021	126.422	126.794
t_c (μs)	1.09462	1.63314	2.16787

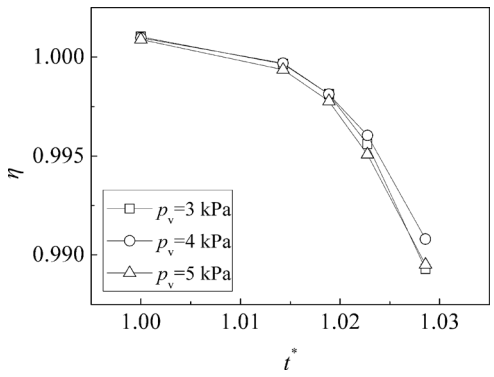

Fig. 10 Changes of dimensionless temperature at the central point of the wall under the different saturated vapor pressures

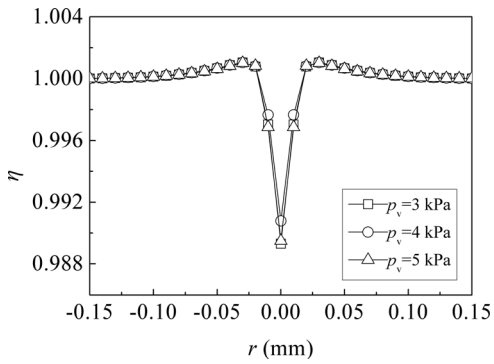

Fig. 11 Distributions of the dimensionless temperature on the solid wall under the different saturated vapor pressures at $t^* = 1.0286$

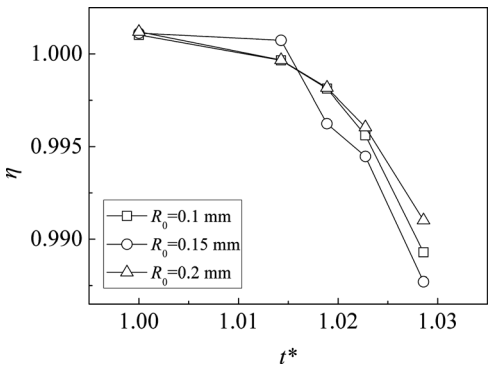

Fig. 12 Changes of the dimensionless temperature at the central point of the wall under the different initial bubble radii

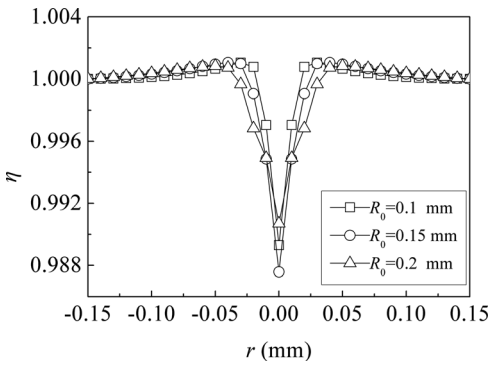

Fig. 13 Distributions of the dimensionless temperature on the solid wall under the different initial bubble radii at $t^* = 1.0286$

velocities and collapse time for the three cases. With the increase of the saturated vapor pressure, the maximum jet velocity on the axis falls to 117.905 m/s from 128.021 m/s. In contrast, the collapse time is extended as the saturated vapor pressure increases. A higher pressure inside the bubble would resist the shrinkage of the bubble interface, which prolongs the collapse time. Thereby, it can be concluded that the cavitation intensity decreases with the increase of initial liquid temperature.

Figure 10 shows the time-dependent changes of η at the central point of the wall under the different saturated vapor pressures. As described in Sec. 5.2, heat transfer has the same situation before the complete collapse for all the saturated vapor pressures. Nevertheless, the situation has slightly changed at the late stage of the collapse, and the heat transfer enhancement has a slight difference between $p_v = 3$ kPa and the other two cases. It should be noted that heat transfer is also enhanced obviously at $p_v = 4$ and 5 kPa. On the whole, the saturated vapor pressure has little effect on the heat transfer enhancement in the present study. Figure 11 shows the distributions of η on the heated wall at $t^* = 1.0286$. It can be seen that the active scope of the microjet has not changed under the different saturated vapor pressures. This demonstrates that the influence of the saturated vapor pressure on the heat transfer enhancement is not obvious again.

5.4 Influence of the Initial Bubble Radius. The simulations were conducted with the initial bubble radii $R_0 = 0.1$ mm, 0.15 mm, 0.2 mm. The other parameters are the same as those in case 1. The maximum jet velocities and collapse time in the three cases are shown in Table 4. It can be seen that the collapse time is significantly extended with the increase of the initial bubble radius. When R_0 is expanded to 0.2 mm from 0.1 mm, the collapse time is nearly doubled and is prolonged to 2.16787 μs from 1.09462 μs. However, the maximum jet velocity has only a slight decline. This indicates the initial bubble radius has a little effect on the collapse strength of the bubble. In spite of this, heat transfer is still affected due to the different distance between the bottom of the bubble and the solid wall, as shown in Fig. 12. The present results show that the heat transfer enhancement has the best effect at $R_0 = 0.15$ mm and the worst effect at $R_0 = 0.20$ mm. Thus, it can be inferred that there is an optimal initial bubble radius to obtain the best enhancing effect. Nevertheless, it should be noted that the active scope of the microjet is expanded for the larger initial bubble radius, as shown in Fig. 13. Moreover, for all the three cases, the ranges of the heat transfer enhancement keep within the corresponding active scope of the microjets. The impingement width of the microjet on the solid wall is about 0.04 mm (-0.02 mm $< r < 0.02$ mm) at $R_0 = 0.1$ mm, 0.06 mm (-0.03 mm $< r < 0.03$ mm) at $R_0 = 0.15$ mm, and

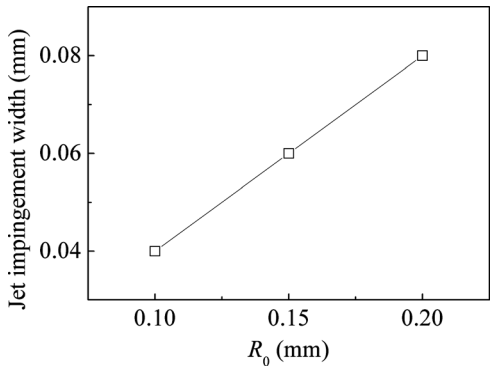

Fig. 14 The impingement width versus the bubble radius

0.08 mm ($-0.04\,\text{mm} < r < 0.04\,\text{mm}$) at $R_0 = 0.2$ mm, as shown in Fig. 14. By analyzing these data, we found that the impingement width of the microjet approximately accounts for twenty percent of the bubble diameter for all the cases. This is a very interesting phenomenon worth further exploration.

6 Conclusions

In the present work, the Navier–Stokes equations and VOF model are employed to study the near-wall cavitation bubble collapse and its effect on the heat transfer. The results show that the bubble collapse is finished in several microseconds time, and the resultant microjet reaches its maximum velocity at the complete collapse moment when the bubble is penetrated. Due to the jet impingement, the wall temperature markedly decreases as well as the thickness of the thermal boundary layer. The maximum velocity of the microjet rises with the increase of the stand-off distance, while the collapse time (t_c) is shortened. These mean that the bubble collapse has higher intensity for a larger stand-off distance. Nevertheless, an excessive long stand-off distance cannot bring the heat transfer enhancement because the impact of the microjet on the solid wall is considerably weakened and even disappears due to the cushioning effect of the liquid. Thus, there is an optimal stand-off distance for the heat transfer enhancement. With the increase of the saturated vapor pressure, the maximum velocity of the microjet falls slightly. In contrast, the collapse time is slightly extended due to a higher pressure inside the bubble. As we know, the vapor pressure corresponds to the liquid temperature. Although the saturated vapor pressure has little effect on the heat transfer enhancement in the present simulated range, it is favorable to keep a lower initial liquid temperature when cavitation is used as an enhanced heat transfer means. The maximum velocity of the microjet nearly maintains unchanged for different initial bubble radius. In spite of this, heat transfer is still affected due to the different distance between the bottom of the bubble and the solid wall. The present results indicate that there is an optimal initial bubble radius to obtain the best enhancing effect. In addition, although the active scope of the microjet is expanded for the larger initial bubble radius, the ratio of the impingement width of the microjet to the bubble diameter always maintains a constant (about 0.2) for all the initial bubble radii. Due to the ever-increasing heat flux in electronic products, the demand for a high-efficiency heat removal system is becoming more intense. In view of its excellent enhancing ability, cavitation has a potential application prospect in the cooling system. According to the related literature, cavitation has been able to be controlled in microfluidic systems [20]. If cavitation bubbles can be produced according to the scale of the microsystem, the cooling capacity of microcooling devices will be greatly improved.

Acknowledgment

This work is financially supported by the National Natural Science Foundation of China (51076151) and the National Basic Research Program of China (2011CB710705).

References

[1] Bergles, A. E., and Newell, P. H., Jr., 1965, "The Influence of Ultrasonic Vibrations on Heat Transfer to Water Flowing in Annuli," Int. J. Heat Mass Transfer, **8**(10), pp. 1273–1280.
[2] Rayleigh, L., 1917, "VIII. On the Pressure Developed in a Liquid During the Collapse of a Spherical Cavity," Philos. Mag. Ser. 6, **34**(200), pp. 94–98.
[3] Plesset, M. S., 1949, "The Dynamics of Cavitation Bubbles," ASME J. Appl. Mech., **16**(277), pp. 228–231.
[4] Gilmore, F. R., 1952, "The Growth or Collapse of a Spherical Bubble in a Viscous Compressible Liquid," California Institute of Technology, Hydrodynamics laboratory, Pasadena, CA, Technical Report No. 26-4.
[5] Plesset, M. S., and Chapman, R. B., 1971, "Collapse of an Initially Spherical Vapour Cavity in the Neighbourhood of a Solid Boundary," J. Fluid Mech., **47**(2), pp. 283–290.
[6] Blake, J. R., and Gibson, D. C., 1987, "Cavitation Bubbles Near Boundaries," Annu. Rev. Fluid Mech., **19**(1), pp. 99–123.
[7] Samiei, E., Shams, M., and Ebrahimi, R., 2010, "Numerical Study on Mass Transfer Effects on Spherical Cavitation Bubble Collapse in an Acoustic Field," ASME Conf. Proc., **2010**(49170), pp. 425–433.
[8] Johnsen, E., and Colonius, T., 2009, "Numerical Simulations of Non-Spherical Bubble Collapse," J. Fluid Mech., **629**, pp. 231–262.
[9] Naude, C. F., and Ellis, A. T., 1961, "On the Mechanism of Cavitation Damage by Non-Hemispherical Cavitations in Contact With a Solid Boundary," ASME J. Basic Eng., **83**, pp. 648–656.
[10] Benjamin, T. B., and Ellis, A. T., 1966, "The Collapse of Cavitation Bubbles and the Pressures Thereby Produced Against Solid Boundaries," Philos. Trans. R. Soc. London, Ser. A, **260**(1110), pp. 221–240.
[11] Tomita, Y., and Shima, A., 1986, "Mechanisms of Impulsive Pressure Generation and Damage Pit Formation by Bubble Collapse," J. Fluid Mech., **169**, pp. 535–564.
[12] Philipp, A., and Lauterborn, W., 1998, "Cavitation Erosion by Single Laser-Produced Bubbles," J. Fluid Mech., **361**, pp. 75–116.
[13] Lauterborn, W., and Ohl, C.-D., 1997, "Cavitation Bubble Dynamics," Ultrason. Sonochem., **4**(2), pp. 65–75.
[14] Yang, S.-H., Jaw, S.-Y., and Yeh, K.-C., 2009, "Single Cavitation Bubble Generation and Observation of the Bubble Collapse Flow Induced by a Pressure Wave," Exp. Fluids, **47**(2), pp. 343–355.
[15] Schneider, B., Kosar, A., Kuo, C.-J., Mishra, C., Cole, G. S., Scaringe, R. P., and Peles, Y., 2006, "Cavitation Enhanced Heat Transfer in Microchannels," J. Heat Transfer, **128**(12), pp. 1293–1301.
[16] Cai, J., Huai, X., Yan, R., and Cheng, Y., 2009, "Numerical Simulation on Enhancement of Natural Convection Heat Transfer by Acoustic Cavitation in a Square Enclosure," Appl. Therm. Eng., **29**(10), pp. 1973–1982.
[17] Cai, J., Huai, X., Liang, S., and Li, X., 2010, "Augmentation of Natural Convective Heat Transfer by Acoustic Cavitation," Fron. Energy Power Eng. China., **4**(3), pp. 313–318.
[18] Brackbill, J. U., Kothe, D. B., and Zemach, C., 1992, "A Continuum Method for Modeling Surface Tension," J. Comput. Phys., **100**(2), pp. 335–354.
[19] Hirt, C. W., and Nichols, B. D., 1981, "Volume of Fluid (VOF) Method for the Dynamics of Free Boundaries," J. Comput. Phys., **39**(1), pp. 201–225.
[20] Zwaan, E., Le Gac, S., Tsuji, K., and Ohl, C.-D., 2007, "Controlled Cavitation in Microfluidic Systems," Phys. Rev. Lett., **98**(25), p. 254501.